

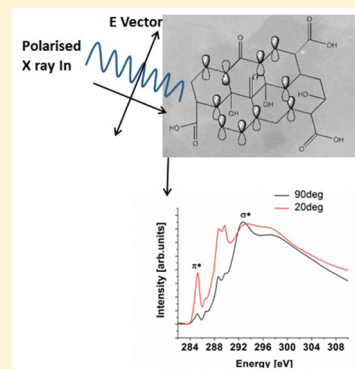
# X-ray Absorption Study of Graphene Oxide and Transition Metal Oxide Nanocomposites

Ram P. Gandhiraman,<sup>\*,†</sup> Dennis Nordlund,<sup>‡</sup> Cristina Javier,<sup>†</sup> Jessica E. Koehne,<sup>†</sup> Bin Chen,<sup>†</sup> and M. Meyyappan<sup>†</sup>

<sup>†</sup>NASA Ames Research Center, Moffett Field, Mountain View, California 94035, United States

<sup>‡</sup>Stanford Synchrotron Radiation Lightsource, Stanford Linear Accelerator Center, Menlo Park, California 94025, United States

**ABSTRACT:** The surface properties of the electrode materials play a crucial role in determining the performance and efficiency of energy storage devices. Graphene oxide and nanostructures of 3d transition metal oxides were synthesized for construction of electrodes in supercapacitors, and the electronic structure and oxidation states were probed using near-edge X-ray absorption fine structure. Understanding the chemistry of graphene oxide would provide valuable insight into its reactivity and properties as the graphene oxide transformation to reduced-graphene oxide is a key step in the synthesis of the electrode materials. Polarized behavior of the synchrotron X-rays and the angular dependency of the near-edge X-ray absorption fine structures (NEXAFS) have been utilized to study the orientation of the  $\sigma$  and  $\pi$  bonds of the graphene oxide and graphene oxide–metal oxide nanocomposites. The core-level transitions of individual metal oxides and that of the graphene oxide nanocomposite showed that the interaction of graphene oxide with the metal oxide nanostructures has not altered the electronic structure of either of them. As the restoration of the  $\pi$  network is important for good electrical conductivity, the C K edge NEXAFS spectra of reduced graphene oxide nanocomposites confirms the same through increased intensity of the  $sp^2$ -derived unoccupied states  $\pi^*$  band. A pronounced angular dependency of the reduced sample and the formation of excitonic peaks confirmed the formation of extended conjugated network.



## INTRODUCTION

Supercapacitors with their superior power density, high discharge/charge rates, and high cyclability compared to batteries are ideal energy storage devices for high-power delivery requirement.<sup>1–3</sup> Graphene with its high electrical conductivity, large surface area, and chemical inertness has been favored for supercapacitor electrodes.<sup>4</sup> Oxidation of graphite and formation of carbonyl functionalities result in an increased interlayer separation. Two-dimensional graphene oxide exfoliated from oxidized graphite possesses an electronic structure similar to that of a wide bandgap semiconductor.<sup>5,6</sup> The presence of  $sp^2$ - and  $sp^3$ -hybridized states in graphene oxide can be altered by either liquid phase or gas phase reduction processes.<sup>7,8</sup> For supercapacitor applications, it is essential to reduce the graphene oxide to obtain electrical double-layer capacitance. The transformation of graphene oxide to reduced-graphene oxide is an important process, and understanding the chemistry of graphene oxide will provide insight into the reactivity and properties of both the graphene oxide and the reduced graphene oxide.<sup>9</sup>

The performance of supercapacitors can be enhanced by using a combination of electrical double-layer capacitance and faradaic capacitance arising through redox charge transfer reactions also called pseudocapacitance.<sup>10,11</sup> The specific capacitance of reduced graphene oxide with 135 F/g could be increased to 480 F/g by incorporating pseudocapacitance materials in the electrode.<sup>12–14</sup> Reduced graphene oxide–metal

oxide nanocomposites as electrode material for supercapacitors has been the topic of intense research, due to the metal oxide pseudocapacitance capabilities that can increase the specific capacitance tremendously. Graphene–metal oxide nanocomposites have shown superior performance as anode materials in lithium ion batteries with high reversible capacities and good cycle performance.<sup>15</sup>  $MnO_2$  with its favorable redox properties results in high pseudocapacitance, and therefore is an excellent candidate for electrode material.<sup>16,17</sup> Graphene oxide–cobalt oxide nanocomposite has also been demonstrated as a highly suitable material for supercapacitor applications exhibiting superior electrochemical behavior and large specific capacitance.<sup>18,19</sup> However, these two materials when used in combination should retain good adhesion, uniform coverage, and good electrical contact with extremely low interface resistance.

A robust electrophoretic deposition (EPD) technique enabled uniform deposition of graphene oxide in the present work. In our earlier work, the EPD process had been optimized to obtain a good adhering film, and also the electrical characteristics of the nanocomposite film were tested using cyclic voltammetry.<sup>20</sup> It is essential to probe the morphology, electronic structure, and orientation of oxide materials to

**Received:** April 22, 2014

**Revised:** June 19, 2014

**Published:** July 18, 2014

improve the electrode performance. Carbon and oxygen core-level spectroscopy, in particular X-ray absorption spectroscopy (XAS), is a very sensitive probe of the local electronic structure as well as chemical composition and local bonding environment,<sup>21</sup> which has been applied in several studies of reduced graphene oxides.<sup>22,23</sup> In this work, XAS is employed to study the surface properties of the individual oxides and the nanocomposites, and the sensitivity of XAS to the local environment is used to identify the various carbon bonding environments. Angular-dependent XAS provides further insight into molecular orientation of local structures in the graphene oxide and nanocomposite.

## ■ EXPERIMENTAL WORK

**Materials Synthesis.** Chemicals used for GO and metal oxide synthesis were purchased from Sigma-Aldrich; 18 MΩ-cm water was used for all experiments. The synthesis protocol is explained in detail in our previous works.<sup>20,24</sup> For GO, MnO<sub>2</sub>, and Co<sub>3</sub>O<sub>4</sub> nanomaterial synthesis, the procedures in refs 25–27 were followed.

GO was synthesized using a modified Hummers' method. The produced GO was suspended in water and then centrifuged at 3800 rpm for 40 min. The supernatant containing 0.75 mg/mL of graphene oxide flakes was reserved for film deposition. MnO<sub>2</sub> nanowires were synthesized solvothermally; 1 mmol of potassium permanganate was mixed with 1 mmol of ammonium chloride and placed in a 45 mL acid digestion bomb (Parr Instruments). The vessel was placed in a 140 °C furnace for 24 h. The synthesized MnO<sub>2</sub> nanowires were cleaned with DI water and ethanol before drying. Cobalt nitrate hexahydrate was dissolved in 10 mL of DI water. Ammonium hydroxide, 28–30%, was slowly added to the solution, stirred for 30 min, and poured into a Petri dish. Stainless steel discs were placed 1 mm horizontally above the bottom of the Petri dish held by two custom-machined PTFE pieces. The Petri dish was covered and placed in a 90 °C furnace for 16 h to produce Co<sub>3</sub>O<sub>4</sub> nanorods.

**Langmuir–Blodgett Film Deposition.** Pieces of silicon wafers were cleaned in a 3:1 sulfuric acid/hydrogen peroxide mixture for 30 min. The cleaned, hydrophilic-rendered wafers were placed in DI water until further use. MnO<sub>2</sub> nanowires and Co<sub>3</sub>O<sub>4</sub> nanorods were separately suspended in methanol at a concentration of 4.5 mg/mL. For the composite films, the GO suspension was sonicated with either MnO<sub>2</sub> or Co<sub>3</sub>O<sub>4</sub> in a 2:1 ratio. A Langmuir–Blodgett (LB) trough (102M, KSV NIMA) was cleaned thoroughly with ethanol and filled with DI water. The wafer was submerged in the trough prior to deposition of the material onto the subphase. The suspensions were slowly added dropwise using a 100 μL pipet for up to 3 mL. Barrier speeds were set at 20 cm<sup>2</sup>/min until the target pressure was reached and the wafer pulled up at a rate of 2 mm/min for all films.

Graphene oxide samples were thermally reduced in a tube furnace (Lindberg/Blue MiniMite) by ramping to 300 °C at a rate of 10 °C/min and then held at the maximum temperature for 30 min before slowly cooling back to room temperature. The annealing temperature of 300 °C was chosen as optimum after several trials of 600 °C for 2 h, 400, 350, and 300 °C. The nanocomposites were found to be damaged at temperatures 400 °C and above, as confirmed by both visual inspection and Raman spectroscopy.

**X-ray Absorption Spectroscopy (XAS).** Ex situ X-ray absorption spectroscopy (XAS, NEXAFS) was performed on

the 31-pole wiggler beamline 10-1 at the Stanford Synchrotron Radiation Lightsource (SSRL) using a ring current of 500 mA. The beamline is equipped with spherical grating monochromator operated with a 1000 lines/mm<sup>-1</sup> grating at 40 μm entrance and exit slits (O 1s XAS, Mn 2p XAS, and Co 2p XAS), providing ~10<sup>11</sup> photons\*s<sup>-1</sup> at about 0.2–0.35 eV resolution in a 1 mm<sup>2</sup> beam spot. Carbon XAS was measured with 600L/mm grating using 30 μm slits, corresponding to about 0.15 eV resolution.

All data were acquired at room temperature and under ultrahigh vacuum (10<sup>-9</sup> torr). Both total electron yield (TEY, measured via the sample drain current) and Auger electron yield (AEY, measured with a cylindrical mirror analyzer) were recorded simultaneously. All spectra were normalized by the incoming flux, measured from a thin grid with freshly evaporated gold, positioned upstream of the sample chamber. A reference sample with several transition metal oxides, intercepting a few percent of the beam upstream and recorded simultaneously, was used to calibrate the energy of the cobalt, manganese, and oxygen scans with a relative energy precision of ±25 meV. Carbon XAS was referenced to the carbon dip which has been calibrated to 284.7 eV using HOPG. All samples were affixed to the aluminum sample holder using conductive carbon tape. Normalized total electron yield data is used throughout the discussion below. The data was normalized to a linear background function at higher energy. When the background subtraction was associated with large error bars, and an additional constraint forcing the area to be the same across several samples was used to get a robust and reliable comparison across samples. SEM imaging was performed using S4800, Hitachi (Pleasanton, CA) scanning electron microscope.

## ■ RESULTS AND DISCUSSION

The surface properties including electronic structure, molecular orientation, and surface morphology play a crucial role in determining the interaction of various materials within the composite and also the interaction of adsorbed molecules with the electrode. The morphology was investigated with SEM imaging, and we have performed X-ray spectroscopy and vibrational spectroscopy to determine local bonding environments and molecular orientations for graphene oxide as well as the nanocomposites. Figure 1a shows the SEM image of planar graphene oxide prepared using electrophoretic deposition indicating a clear planar surface with no agglomeration, and the corresponding C and O K edge XAS is shown in Figure 2a

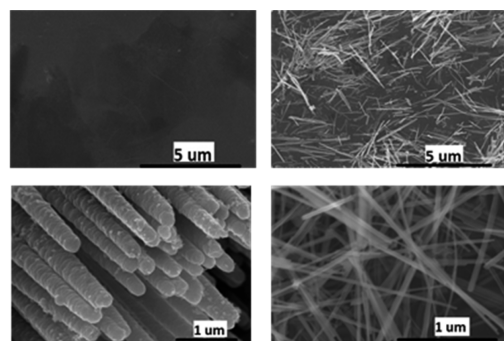


**Figure 1.** SEM image of (top left, a) graphene oxide; (top right, b) graphene oxide–manganese oxide nanocomposite; (bottom left, c) cobalt oxide nanorods; (bottom right, d) manganese oxide nanowires.

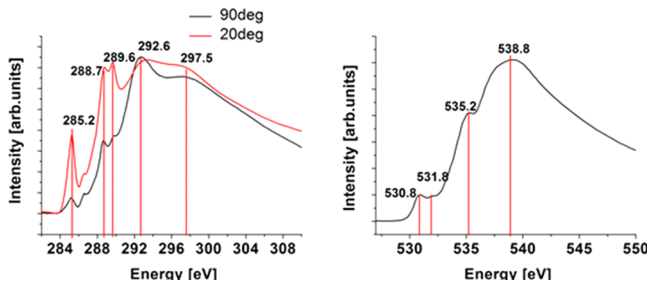


**Figure 2.** (Left, a) C 1s NEXAFS spectra of graphene oxide measured at X-ray incident angles 20° and 90°; (right, b) O 1s NEXAFS spectra of graphene oxide measured at X-ray incident angle 54°.

and Figure 2b, respectively. The graphene oxide–manganese oxide nanocomposite prepared using the Langmuir–Blodgett deposition is shown in Figure 1b in which the nanowires with varying diameters from 30 to 60 nm are clearly seen.  $\text{Co}_3\text{O}_4$  nanorods in Figure 1c are over 10  $\mu\text{m}$  in length, and solvothermally prepared  $\text{MnO}_2$  nanowires shown in Figure 1d are 30–60 nm in diameter and 3–5  $\mu\text{m}$ . The corresponding L edge XAS plots for the Mn and Co metal oxides and the nanocomposites are in Figure 4a and Figure 4b.

The supercapacitance of the graphene material arises because it can store the electrostatic charges from the electrolytes by simple adsorption, which is reversible (electrical double-layer capacitance). Graphene, with its large surface area and the ability to adsorb molecules reversibly on its surface, offers a unique advantage. As a large surface area of graphene oxide is essential for enhanced specific capacitance, it is essential to have nonagglomerated graphene layers.

X-ray absorption spectroscopy is a powerful probe of the electronic structure in which a tunable X-ray source is used to excite core electrons into unoccupied bound or continuum states. Apart from its elemental specificity, XAS is particularly sensitive to the local electronic structure, including angular anisotropy in molecular orientation, bond length, oxidation state, and symmetry, as well as spin.<sup>28–30</sup> XAS analysis is highly relevant as the information obtained corresponds to a depth of few nanometers into the surface and not to the bulk. Figure 2a shows the C K edge absorption spectra of graphene oxide taken at grazing and normal incidence, showing the  $\text{sp}^2$ -derived unoccupied  $\pi^*$  and  $\sigma^*$  bands at 285.2 and 292.6 eV.<sup>31,32</sup> The relatively broad  $\sigma^*$  resonance and the absence of a core-exciton at around 291.65 eV<sup>33,34</sup> indicate that the  $\text{sp}^2$  network in graphene is substantially defective, as expected. The resonances at 286.5, 288.7, and 289.6 eV correspond to states where the local  $\text{sp}^2$  bonding configuration has been interrupted by (mainly) oxygen functionalization. In particular, double-bonded oxygen functionalization gives rise to a  $\pi^*$  intensity associated with the C=O bond. This carbonyl  $\pi^*$  energy position will be shifted depending on the electronegativity of the local environment around the carbon (e.g., carbonyl C=O in COOH around 288.5, whereas C=O in a ketone environment is found at lower energies).<sup>35,36</sup> Also,  $\text{sp}^2$  or aromatic carbon with some single bond oxygen functionalization such as hydroxyl (phenol, -OH) and epoxy groups (C-O-C) will shift the  $\pi^*$  resonance from the aromatic core up by about 1–2 eV (for that particular carbon atom).<sup>32</sup> In the spectra in Figure 2a, the absorption edge at 285.2 eV corresponds to excitation of carbon in the  $\text{sp}^2$  network into the  $\pi^*$  band, and the peak at 286.5 eV is assigned to  $\pi^*$  excitations for carbon that are single bonded to oxygen (C–O) either in hydroxyl (phenol) or epoxy

configurations, consistent with previous studies on graphene oxide.<sup>37–39</sup> The peak at 288.7 eV corresponds to C=O  $\pi^*$  resonances in carboxyl groups (COOH).<sup>28,32,35</sup> Unfortunately, the literature on carbon XAS cannot give conclusive assignment of the 289.6 eV feature, but we hypothesize that it is associated with Rydberg mixed OH-derived states from hydroxylated and ether-linked C-species (–O–C–OH) based on XAS of carbohydrates and amino sugars by Solomon et al.,<sup>40</sup> as well as EELS studies by Hitchcock et al. of alcohols and other OH-derived functional groups.<sup>32,41</sup> The main  $\sigma^*$  resonance for the uninterrupted  $\text{sp}^2$  network is 292.6 eV, and there is a  $\sigma^*$  resonance attributed to single-bonded oxygen at 297.5 eV, but due to the strong functionalization and interference with many states, the C=O sigma feature from carboxyl expected at around 303 eV cannot be well resolved.

The high linearly polarized nature of synchrotron radiation is a powerful probe of molecular orientations, in particular for light element 1s  $\rightarrow$  2p excitations, where the product of the electric dipole and the orbital symmetry axis gives rise to simple intensity relations between molecular orientation and incidence angle of the radiation (or e-vector).<sup>28,42,43</sup> The NEXAFS spectrum in Figure 2a is a C K edge absorption spectrum collected with a grazing incidence angle of 20° and 90° relative to surface, where for 90° the X-ray (e-vector) is parallel (perpendicular) to the surface normal (corresponding to in-plane excitation). In graphene, the  $\sigma$  band is oriented along the intermolecular bonding axes (in-plane) and the  $\pi$  band is derived from  $p_z$  orbitals oriented perpendicular to graphene plane (out-of-plane). For in-plane excitation (90°) the  $\sigma^*$  resonance is stronger, and the  $\pi^*$  resonance is suppressed, whereas for out-of-plane excitation the opposite is found, as expected. We note that the angular dependence is distinct but rather weak compared to high-quality pristine graphene<sup>44</sup> due to defects and oxygen functionalization that interrupt the stoichiometric  $\text{sp}^2$  network. The C=O resonance shows the same angular dependence as the  $\text{sp}^2$  network, indicating that the C=O bond is primarily in-plane, e.g., pointing into the hollow space created by defects. In contrast, the C–O  $\sigma^*$  resonance at around 297.5 eV shows opposite behavior to the  $\text{sp}^2$ -derived  $\sigma^*$ , indicating that those C–O bonds are primarily directed out-of-plane, as expected for OH phenol groups on top of  $\text{sp}^2$  carbon. The absorption feature at 286.5 eV corresponding to  $\pi^*$  excitations for carbons that are single bonded to oxygen (C–O) either in hydroxyl (phenol) or epoxy configurations do not show observable angular dependency. A similar observation by Jesus et al. on XAS mapping of chemical domains on graphene oxide<sup>45</sup> indicates that for the functional groups that decorate the basal plane and edges of the graphene oxide sheets, the resonances are observed in all due to elimination of angular dependence of intensity induced by the steric orientations of different functional groups.

The O 1s XAS spectra for graphene oxide in Figure 2b display four main resonances at around 530.8, 531.8, 535.2 eV and a convolution of multiple peaks centered around 538.8 eV. The lower absorption edges 530.8 and 531.8 eV are  $\pi^*$  resonances from oxygen double bonded to carbon (carbonyl, C=O).<sup>23,28,32,35,39,46</sup> Based on the C 1s XAS, we associate this intensity mainly with carboxylic groups. There is an associated C=O  $\sigma^*$  intensity at around 539 eV which is not well resolved. The shoulder at 535 eV is a hydroxyl-derived state  $\sigma^*$  (O–H),<sup>32,47,48</sup> and the broad feature around 537.5 eV, which again is not well resolved, is attributed to single-bonded oxygen (e.g., C–OH and C–O–C)  $\sigma^*$  based on the vast literature on

various alcohols and esters by Hitchcock et al.,<sup>32,46</sup> as well as the agreement with in-vacuum annealed graphene oxide, shown to be dominated by phenolic groups and with much reduced COOH functionality.<sup>39,49,50</sup> Both the C 1s and O 1s spectra are consistent with a hydroxide-rich surface with a mixture of carboxylic and other OH-derived functionalities.

Figure 3 displays the C K edge spectra of graphene oxide and the graphene oxide nanocomposites taken at grazing ( $20^\circ$ ),

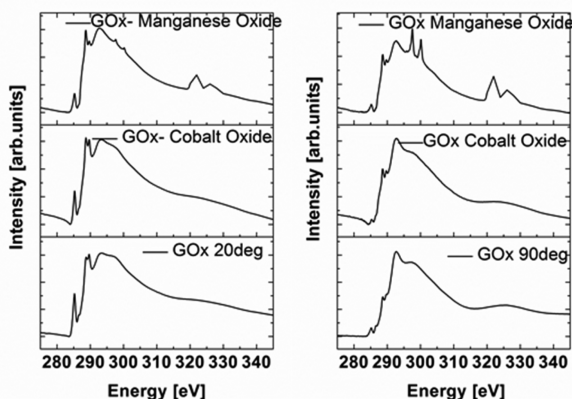


**Figure 3.** C 1s XAS spectra of graphene oxide, graphene oxide–cobalt oxide nanocomposite, and graphene oxide–manganese oxide nanocomposites measured at  $20^\circ$  incidence (left, a) and  $90^\circ$  incidence (right, b).

Figure 3a) and normal incidence ( $90^\circ$ , Figure 3b) relative to the sample surface. The absorption edge at 285.2 eV corresponding to excitation of carbon in the  $\text{sp}^2$  network into the  $\pi^*$  band shows significant variation in intensity with incidence angle of the radiation, for all the samples, demonstrating the out of plane orientation of  $\pi$  band. Overall, we find that the graphene in the nanocomposite mainly retains its structure and angular dependence with some subtle differences. There is some residual potassium L edge peaks at 297.5 and 300.2 eV corresponding to 2p3/2 and 2p1/2 transitions in Figure 3b (top), indicating the incorporation of K<sup>+</sup> ions in the graphene oxide–manganese oxide composite.<sup>51,52</sup> The presence of K 2p peaks on electrophoretically deposited graphene oxide films reduced using KOH/hydrazine has been reported by Lee et al.<sup>38</sup>

In Figure 3a, at  $20^\circ$  incident angle, the absorption edge intensity ratio  $\pi^*288.7 \text{ eV}/\pi^*289.6 \text{ eV}$  is higher for graphene oxide–manganese oxide nanocomposite compared to graphene oxide–cobalt oxide nanocomposite and graphene oxide. This is accompanied by a suppression of the sigma star intensity at around 297 eV. We associate the second resonance with OH moieties (i.e., O–C–OH) and also the intensity of the C–O  $\sigma^*$  at 297 eV. The sonication in MnO<sub>2</sub>/methanol suspension alters the GO slightly to reduce the OH functionalization.

To investigate the electronic structure of the Mn oxide and Co oxide nanoparticles, we acquired Mn 2p (Figure 4a) and Co 2p (Figure 4b) XAS. L-edge XAS of transition metal oxides is a sensitive probe of oxidation and symmetry through the direct dipole transition into the unoccupied frontier orbitals.<sup>53</sup> Cramer et al., in their XAS analysis of manganese L edge, reported that the L2,3 edge features of transition metal complex that involve 2p–3d transitions are sharper, richer, and much more sensitive in oxidation state determination than the K-edge features which are broad.<sup>54</sup> Further, it was well established that

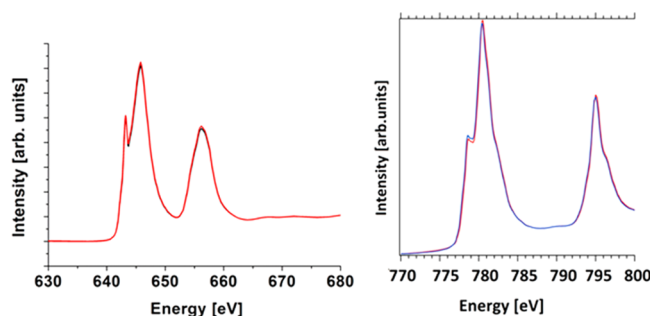


**Figure 4.** L-edge (2p) XAS of (left, a) Mn in manganese oxide NW (black curve) and graphene oxide–manganese oxide nanocomposite (red curve) and (right, b) Co in cobalt oxide NR (red curve) and graphene oxide–cobalt oxide nanocomposite (blue curve).

Mn L edge absorptions are dominated by Mn 3d states and hence an excellent indicator of oxidation state and coordination.<sup>55</sup> In particular, different oxidation states are typically discriminated by simple comparisons with powder references. All L-edge XAS spectra are shown in an extended region covering both the L3 (2p3/2) and the L2 (2p1/2), displaying a large spin-orbit splitting.

The energy position, peak separation, and relative intensity of the peak in Mn L-edge spectrum of the nanowires matches that of MnO<sub>2</sub>.<sup>56,57</sup> Co L edge XAS confirms that the Co is found in a trivalent configuration<sup>58</sup> resembling the spinel Co<sub>3</sub>O<sub>4</sub> structure with octahedrally coordinated Co<sup>3+</sup> and Co<sup>2+</sup> cations tetrahedrally coordinated with oxygen. The cobalt oxide nanostructures with varying oxidation states and crystal structures are known to exhibit different electrochemical behavior.<sup>59</sup> Moreover, the L-edge XAS spectra of both oxides and their corresponding nanocomposite with graphene oxide are exactly the same with no observable difference in the absorption edges, demonstrating that the manganese oxide and cobalt oxide retain their crystal symmetry and electronic configuration in the nanocomposites. Studies on the oxidation states of cobalt have demonstrated that the accumulation of chemisorbed oxygen and diffusion results in the formation of surface oxide.<sup>60</sup> Co<sub>3</sub>O<sub>4</sub> is a stable form of oxide, and the observed similarity in the XAS spectra of cobalt oxide and the composite shows that there is no variation in the electronic structure. In graphene composites, the stacking between individual graphene sheets is driven by strong  $\pi$ – $\pi$  interaction, and the metal oxide nanostructures are surface anchored to the graphene through van der Waals force.<sup>18,61</sup>

The C K edge absorption spectra of reduced graphene oxide (Figure 5a) and reduced graphene oxide–cobalt oxide nanocomposite (Figure 5b) taken at grazing and normal incidence show a distinct difference from that of graphene oxide shown in Figure 2a. The absorption edge at 285.2 eV corresponding to excitation of carbon in the  $\text{sp}^2$  network into the  $\pi^*$  band shows a distinct and strong angular dependency. A strong 289.6 eV feature observed for graphene oxide that we attributed to Rydberg mixed OH-derived states from hydroxylated and ether-linked C-species (–O–C–OH) is missing in the reduced graphene oxide, indicating that the hydroxylated species are removed upon heat treatment. This will invariably alter the electronic structure of the reduced graphene oxide, and the consequence of this change can be observed by comparing the peak position of the carbonyl (C=O)  $\pi^*$  resonance before and after reduction. In graphene oxide, the peak at 288.7 eV corresponds to C=O  $\pi^*$  resonances in

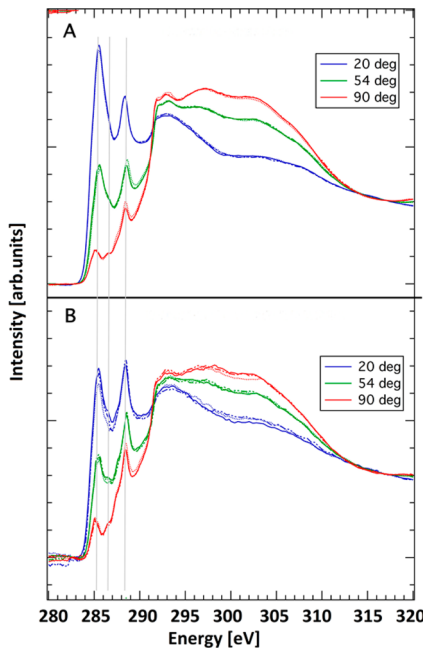


**Figure 5.** C 1s NEXAFS spectra of (top, a) reduced graphene oxide and (bottom, b) reduced graphene oxide–cobalt oxide nanocomposites measured at incident angles 20°, 54°, and 90°.

carboxyl groups (COOH). The carbonyl  $\pi^*$  resonance position has shifted by 0.3 eV to lower energy for reduced graphene oxide (from 288.7 to 288.4 eV). This peak position is consistent with trends in positions of C 1s to  $\pi^*$  C=O transitions as a function of electronegativity of the substituents, studied in solid state and by computational methods by Urquhart and Ade.<sup>35</sup> The removal of hydroxyl groups bonded to the carbonyl carbon actually results in the removal of electronegative oxygen, the presence of which increases the position of  $\pi^*$  resonance of carbonyl carbon. Another important aspect observed in the reduced graphene oxide is the ratio of intensities of  $\pi^*$  excitation of carbon in the  $sp^2$  network to that of  $\sigma^*$  resonance around 292.6 eV and the ratio of  $\pi^*$  excitation of carbon in the  $sp^2$  to that of  $\pi^*$  resonance of carbonyl carbon. An enormous increase in intensity of  $sp^2$ -derived unoccupied  $\pi^*$  resonance is observed for reduced graphene oxide suggesting substantial restoration of the  $\pi$  conjugated network. Unlike the graphene oxide, the angular dependency is very strong and evident for reduced sample. Appearance of excitonic peak at 291.7 eV and the doublet nature of this excitonic peak with an additional peak around 292.8 eV further confirm the formation of extended conjugated network.<sup>33,37</sup>

In our earlier work<sup>20</sup> we studied the changes in chemical structure of graphene oxide upon reduction and observed the following: (i) both the D-band and G-band peaks were shifted to lower wavenumbers, and the shift of the D-band peak was noticeably larger than that of the G-band peak; (ii) the D bandwidth decreased; and (iii) the change in the relative intensity of the D and G band with D/G ratio calculated with integrated peak areas changed from 0.7:1 to 2.6:1 from GO to rGO. The observed change in the C K edge XAS spectra of graphene oxide upon reduction is similar to the changes observed in our Raman studies. Overall, the reduced graphene oxide has more graphene-like behavior.

As the temperature used for reducing graphene oxide is 300 °C, Co<sub>3</sub>O<sub>4</sub> is stable in this temperature region.<sup>62</sup> The good contact between the graphene oxide and the nanostructured materials in the composite film produced by Langmuir–Blodgett process ensures low contact resistance and good adhesion between them as evident from previous electrochemical studies.<sup>20</sup> He et al.<sup>63</sup> reported that the large surface area of graphene and the efficient use of the pseudocapacitive nanomaterial (MnO<sub>2</sub>) for charge storage leads to remarkable electrochemical performance with high specific capacitance and extended cycling performance.

## CONCLUSION

Graphene oxides and nanostructures of 3d transition metal oxides with various geometries (cobalt oxide nanorods, manganese oxide nanowire) were synthesized for using as electrode material in supercapacitors. The fundamental understanding on the coordination symmetry, oxidation station, and interactions of the neighboring compounds in a composite can lead to optimization of the material characteristics which in turn could result in an enhanced device performance. As most reactions take place at the surface, studying electronic structure and the surface chemical properties are crucial. XAS spectroscopic measurements carried out to study the oxidation state and the bonding environments of the nanocomposites showed that the electronic structure and the oxidation state of the metal oxides remain the same in the nanocomposite. Upon thermal reduction, the  $sp^2$ -hybridized framework of graphene is restored while removing the electronegative functionalities that reduce the electrical charge carrier transportation to a significant extent. Thermal reduction of the graphene oxide and the nanocomposite resulted in major changes like sharp increase in the angular dependency of the C K edge spectra, increased intensity of the  $sp^2$ -derived unoccupied band, removal of hydroxyl states, and the appearance of excitonic state, all of which confirm favorable change in electronic structure for supercapacitor applications.

## AUTHOR INFORMATION

### Corresponding Author

\*E-mail: ramprasad.gandhiraman@nasa.gov. Phone: +1 650 604 4702.

### Notes

The authors declare no competing financial interest.

## ACKNOWLEDGMENTS

R.P.G. is with Universities Space Research Association subcontracted to NASA Ames Research Center under NASA cooperative agreement. The beam time for synchrotron measurements was awarded to the authors through the peer-reviewed SLAC research proposal No. 2163. Use of the Stanford Synchrotron Radiation Lightsource, SLAC National Accelerator Laboratory, is supported by the U.S. Department of Energy, Office of Science, Office of Basic Energy Sciences under Contract No. DE-AC02-76SF00515. The SSRL Structural Molecular Biology Program is supported by the DOE Office of Biological and Environmental Research and by the National Institutes of Health, National Institute of General Medical Sciences (including P41GM103393). The contents of this publication are solely the responsibility of the authors and do not necessarily represent the official views of NIGMS or NIH.

## ■ REFERENCES

(1) Meyyappan, M. Nanostructured Materials for Supercapacitors. *J. Vac. Sci. Technol., A* **2013**, *31*, 050803–1.

(2) Simon, P.; Gogotsi, Y. Materials for Electrochemical Capacitors. *Nat. Mater.* **2008**, *7*, 845–854.

(3) Miller, J. R.; Simon, P. Electrochemical Capacitors for Energy Management. *Science* **2008**, *321*, 651–652.

(4) Liu, C.; Yu, Z.; Neff, D.; Zhamu, A.; Jang, B. Z. Graphene-Based Supercapacitor with an Ultrahigh Energy Density. *Nano Lett.* **2010**, *10*, 4863–4868.

(5) Saxena, S.; Tyson, T. A.; Negusse, E. Investigation of the Local Structure of Graphene Oxide. *J. Phys. Chem. Lett.* **2010**, *1*, 3433–3437.

(6) Prezhdo, O. V.; Kamat, P. V.; Schatz, G. C. Virtual Issue: Graphene and Functionalized Graphene. *J. Phys. Chem. C* **2011**, *115*, 3195–3197.

(7) Gómez-Navarro, C.; Weitz, R. T.; Bittner, A. M.; Scolari, M.; Mews, A.; Burghard, M.; Kern, K. Electronic Transport Properties of Individual Chemically Reduced Graphene Oxide Sheets. *Nano Lett.* **2007**, *7*, 3499–3503.

(8) Stankovich, S.; Dikin, D. A.; Piner, R. D.; Kohlhaas, K. A.; Kleinhammes, A.; Jia, Y.; Wu, Y.; Nguyen, S. T.; Ruoff, R. S. Synthesis of Graphene-Based Nanosheets via Chemical Reduction of Exfoliated Graphite Oxide. *Carbon* **2007**, *45*, 1558–1565.

(9) Dreyer, D. R.; Park, S.; Bielawski, C. W.; Ruoff, R. S. The Chemistry of Graphene Oxide. *Chem. Soc. Rev.* **2010**, *39*, 228–240.

(10) Simon, P.; Gogotsi, Y. Materials for Electrochemical Capacitors. *Nat. Mater.* **2008**, *7*, 845–854.

(11) Yu, G.; Hu, L.; Liu, N.; Wang, H.; Vosgueritchian, M.; Yang, Y.; Cui, Y.; Bao, Z. Enhancing the Supercapacitor Performance of Graphene/MnO<sub>2</sub> Nanostructured Electrodes by Conductive Wrapping. *Nano Lett.* **2011**, *11*, 4438–4442.

(12) Zhang, L. L.; Zhou, R.; Zhao, X. S. Graphene-Based Materials as Supercapacitor Electrodes. *J. Mater. Chem.* **2010**, *20*, 5983–5992.

(13) Liu, J.; Jiang, J.; Cheng, C.; Li, H.; Zhang, J.; Gong, H.; Fan, H. J. Co<sub>3</sub>O<sub>4</sub> Nanowire@MnO<sub>2</sub> Ultrathin Nanosheet Core/Shell Arrays: A New Class of High Performance Pseudocapacitive Materials. *Adv. Mater.* **2011**, *23*, 2076–2081.

(14) Zhang, L. L.; Zhao, X. S. Carbon-Based Materials as Supercapacitor Electrodes. *Chem. Soc. Rev.* **2009**, *38*, 2520.

(15) Yu, A.; Park, H. W.; Davies, A.; Higgins, D. C.; Chen, Z.; Xiao, X. Free-Standing Layer-by-Layer Hybrid Thin Film of Graphene–MnO<sub>2</sub> Nanotube as Anode for Lithium Ion Batteries. *J. Phys. Chem. Lett.* **2011**, *2*, 1855–1860.

(16) Lake, J. R.; Cheng, A.; Selverston, S.; Tanaka, Z.; Koehne, J.; Meyyappan, M.; Chen, B. Graphene Metal Oxide Composite Supercapacitor Electrodes. *J. Vac. Sci. Technol., B* **2012**, *30* (3), 03D118–6.

(17) Choi, B. G.; Yang, M.; Hong, W. H.; Choi, J. W.; Huh, Y. S. 3D Macroporous Graphene Frameworks for Supercapacitors with High Energy and Power Densities. *ACS Nano* **2012**, *6*, 4020–4028.

(18) Dong, X.-C.; Xu, H.; Wang, X.-W.; Huang, Y.-X.; Chan-Park, M. B.; Zhang, H.; Wang, L.-H.; Huang, W.; Chen, P. 3D Graphene–Cobalt Oxide Electrode for High-Performance Supercapacitor and Enzymeless Glucose Detection. *ACS Nano* **2012**, *6*, 3206–3213.

(19) Yan, J.; Fan, Z. J.; Wei, T.; Qian, W. Z.; Zhang, M. L.; Wei, F. Reduction of Graphene Oxide by an In-Situ Photoelectrochemical Method in a Dye-Sensitized Solar Cell Assembly. *Carbon* **2010**, *48*, 3825–3833.

(20) Lake, J. R.; Cheng, A.; Selverston, S.; Tanaka, Z.; Koehne, J.; Meyyappan, M.; Chen, B. Graphene Metal Oxide Composite Supercapacitor Electrodes. *J. Vac. Sci. Technol., B* **2012**, *30* (3), 03D118–6.

(21) Benny, T. H.; Banerjee, S.; Sambasivan, S.; Balasubramanian, M.; Fischer, D. A.; Eres, G.; Puretzky, A. A.; Geohegan, D. B.; Lowndes, D. H.; Han, W.; et al. Near-Edge X-ray Absorption Fine Structure Spectroscopy as a Tool for Investigating Nanomaterials. *Small* **2006**, *2* (1), 26–35.

(22) Schultz, B. J.; Patridge, C. J.; Lee, V.; Jaye, C.; Lysaght, P. S.; Smith, C.; Barnett, J.; Fischer, D. A.; Prendergast, D.; Banerjee, S. Imaging Local Electronic Corrugations and Doped Regions in Graphene. *Nat. Commun.* **2011**, *2*, 372/1–8.

(23) Lee, V.; Whittaker, L.; Jaye, C.; Baroudi, K. M.; Fischer, D. A.; Banerjee, S. Large-Area Chemically Modified Graphene Films: Electrophoretic Deposition and Characterization by Soft X-ray Absorption Spectroscopy. *Chem. Mater.* **2009**, *21*, 3905–3916.

(24) Gutierrez, D. H.; Lake, J.; Javier, C.; Cheng, A.; Tanaka, Z.; Londoño, N. J.; Chen, B. Phoretic Deposition of Graphene on Manganese–Cobalt Oxide Composites for Supercapacitor Electrodes. *Adv. Sci. Technol.* **2013**, *77*, 302–306.

(25) An, S. J.; Zhu, Y.; Lee, S. H.; Stoller, M. D.; Emilsson, T.; Park, S.; Velamakanni, A.; An, J.; Ruoff, R. S. Thin Film Fabrication and Simultaneous Anodic Reduction of Deposited Graphene Oxide Platelets by Electrophoretic Deposition. *J. Phys. Chem. Lett.* **2010**, *1*, 1259–1263.

(26) Gao, Y.; Wang, Z.; Wang, J.; Zou, G.; Qian, Y. A Facile Route to Synthesize Uniform Single-Crystalline α-MnO<sub>2</sub> Nanowires. *J. Cryst. Growth* **2005**, *279*, 415–419.

(27) Li, Y.; Tan, B.; Wu, Y. Mesoporous Co<sub>3</sub>O<sub>4</sub> Nanowire Arrays for Lithium Ion Batteries with High Capacity and Rate Capability. *Nano Lett.* **2008**, *1*, 265–270.

(28) Stohr, J. *NEXAFS Spectroscopy*; Springer: New York, 1992.

(29) Groot, F. D.; Kotani, A. *Core Level Spectroscopy of Solids*; CRC Press: Boca Raton, FL, 2008.

(30) Hahner, G. Near Edge X-ray Absorption Fine Structure Spectroscopy as a Tool To Probe Electronic and Structural Properties of Thin Organic Films and Liquids. *Chem. Soc. Rev.* **2006**, *35*, 1244–1255.

(31) Urquhart, S.; Hitchcock, A. P.; Priester, R. D.; Rightor, E. G. Analysis of Polyurethanes Using Core Excitation Spectroscopy. Part II: Inner Shell Spectra of Ether, Urea, and Carbamate Model Compounds. *J. Polym. Sci., Part B: Polym. Phys.* **1995**, *33*, 1603–1620.

(32) Ishii, I.; Hitchcock, A. P. The Oscillator Strengths for Cls and Ols Excitation of Some Saturated and Unsaturated Organic Acids, Alcohols, and Esters. *J. Electron Spectrosc. Relat. Phenom.* **1988**, *46*, 55–64.

(33) Bruhwiler, P. A.; Maxwell, A. J.; Puglia, C.; Nilsson, A.; Anderson, S.; Martensson, N. π\* and σ\* Excitons in C 1s Absorption of Graphite. *Phys. Rev. Lett.* **1995**, *74* (4), 614–7.

(34) Ahuja, R.; Bruhwiler, P. A.; Wills, J. M.; Johansson, B.; Martensson, N.; Eriksson, O. Theoretical and Experimental Study of the Graphite 1s X-ray Absorption Edges. *Phys. Rev. B* **1996**, *54* (20), 14396–404.

(35) Urquhart, S. G.; Ade, H. Trends in the Carbonyl Core (C 1s, O 1s) → π\*C=O Transition in the Near-Edge X-ray Absorption Fine Structure Spectra of Organic Molecules. *J. Phys. Chem. B* **2002**, *106*, 8531–8538.

(36) Lessard, R.; Cuny, J.; Cooper, G.; Hitchcock, A. P. Inner-Shell Excitation of Gas Phase Carbonates and a,c-Dicarbonyl Compounds. *Chem. Phys.* **2007**, *331*, 289–303.

(37) Dennis, R. V.; Schultz, B. J.; Jaye, C.; Wang, X.; Fischer, D. A.; Cartwright, A. N.; Banerjee, S. Near-Edge X-ray Absorption Fine Structure Spectroscopy Study of Nitrogen Incorporation in Chemically Reduced Graphene Oxide. *J. Vac. Sci. Technol., B* **2013**, *31* (4), 041204–1–9.

(38) Lee, V.; Whittaker, L.; Jaye, C.; Baroudi, K. M.; Fischer, D. A.; Banerjee, S. Large-Area Chemically Modified Graphene Films: Electrophoretic Deposition and Characterization by Soft X-ray Absorption Spectroscopy. *Chem. Mater.* **2009**, *21*, 3905–3916.

(39) Ganguly, A.; Sharma, S.; Papakonstantinou, P.; Hamilton, J. Probing the Thermal Deoxygenation of Graphene Oxide Using High-Resolution In Situ X-ray-Based Spectroscopies. *J. Phys. Chem. C* **2011**, *115*, 17009–17019.

(40) Solomon, D.; Lehmann, J.; Kinyangi, J.; Liang, B.; Schafer, T. Carbon K-Edge NEXAFS and FTIR-ATR Spectroscopic Investigation of Organic Carbon Speciation in Soils. *Soil. Sci. Soc. Am. J.* **2005**, *69*, 107–119.

(41) Hitchcock, A. P.; Mancini, D. C. Bibliography and Database of Inner-Shell Excitation Spectra of Gas Phase Atoms and Molecules. *J. Electron Spectrosc.* **1994**, *67*, 1–123.

(42) Stöhr, J.; Outka, D. A. Determination of Molecular Orientations on Surfaces from the Angular Dependence of Near-Edge X-ray Absorption Fine Structure Spectra. *Phys. Rev. B* **1987**, *36*, 7891.

(43) Lee, V.; Dennis, R. V.; Schultz, B. J.; Jaye, C.; Fischer, D. A.; Banerjee, S. Soft X-ray Absorption Spectroscopy Studies of the Electronic Structure Recovery of Graphene Oxide upon Chemical Defunctionalization. *J. Phys. Chem. C* **2012**, *116*, 20591–20599.

(44) Schiros, T.; Nordlund, D.; Palova, L.; Prezzi, D.; Zhao, L.; Kim, K. S.; Wurstbauer, U.; Gutierrez, C.; Delongchamp, D.; Jaye, C.; et al. Connecting Dopant Bond Type with Electronic Structure in N-Doped Graphene. *Nano Lett.* **2012**, *12*, 4025–4031.

(45) Jesus, L. R. D.; Dennis, R. V.; Depner, S. W.; Jaye, C.; Fischer, D. A.; Banerjee, S. Inside and Outside: X-ray Absorption Spectroscopy Mapping of Chemical Domains in Graphene Oxide. *J. Phys. Chem. Lett.* **2013**, *4*, 3144–3151.

(46) Outka, D. A.; Stohr, J.; Madix, R. J.; Rotermund, H. H.; Hermansmeier, B.; Solomon, J. NEXAFS Studies of Complex Alcohols and Carboxylic Acids on the Si(111)(7 × 7) Surface. *Surf. Sci.* **1987**, *18S*, 53–74.

(47) Francis, J. T.; Hitchcock, A. P. Inner-Shell Spectroscopy of *p*-Benzoquinone, 1,3-Cyclohexandione, *p*-Hydroxyquinone, and Phenol: Quinoid versus Aromaticity as Viewed by the Unoccupied Orbitals. *J. Phys. Chem.* **1992**, *96*, 6598–6610.

(48) Pacilé, D.; Meyer, J. C.; Rodríguez, A. F.; Papagno, M.; Gómez-Navarro, C.; Sundaram, R. S.; Burghard, M.; Kern, K.; Carbone, C.; Kaiser, U. Electronic Properties and Atomic Structure of Graphene Oxide Membranes. *Carbon* **2011**, *49*, 966.

(49) Benny, T. H.; Banerjee, S.; Sambasivan, S.; Balasubramanian, M.; Fischer, D. A.; Eres, G.; Puretzky, A. A.; Geoghegan, D. B.; Lowndes, D. H.; Han, W.; et al. Near-Edge X-ray Absorption Fine Structure Spectroscopy as a Tool for Investigating Nanomaterials. *Small* **2006**, *2* (1), 26–35.

(50) Schultz, B. J.; Patridge, C. J.; Lee, V.; Jaye, C.; Lysaght, P. S.; Smith, C.; Barnett, J.; Fischer, D. A.; Prendergast, D.; Banerjee, S. Imaging Local Electronic Corrugations and Doped Regions in Graphene. *Nat. Commun.* **2011**, *2*, 372/1–8.

(51) Richter, C.; Jaye, C.; Panaitescu, E.; Fischer, D. A.; Lewis, L. H.; Willey, R. J.; Menon, L. Effect of Potassium Adsorption on the Photochemical Properties of Titania Nanotube Arrays. *J. Mater. Chem.* **2009**, *19*, 2963.

(52) Nelson, A. J.; van Buren, T.; Miller, E.; Land, T. A.; Bostedt, C.; Franco, N.; Whitman, P. K.; Baisden, P. A.; Terminello, L. J.; Callcott, T. A. X-ray Absorption Analysis of KDP Optics. *J. Electron Spectrosc. Relat. Phenom.* **2001**, *114–116*, 873–878.

(53) de Groot, F. M. F.; Fuggle, J. C.; Thole, B. T.; Sawatzky, G. A. 2p X-ray Absorption of 3d Transition-Metal Compounds: An Atomic Multiplet Description Including the Crystal Field. *Phys. Rev. B* **1990**, *42*, 5459–5468.

(54) Cramer, S. P.; deCroot, F. M. F.; Ma, Y.; Chen, C. T.; Sette, F.; Kipke, C. A.; Eichhorn, D. M.; Chan, M. K.; Armstrong, W. H.; Libby, E.; et al. Ligand Field Strengths and Oxidation States from Manganese L-Edge Spectroscopy. *J. Am. Chem. Soc.* **1991**, *113*, 7937–7940.

(55) Grush, M. M.; Chen, J.; Stemmler, T. L.; George, S. J.; Ralston, C. Y.; Stirbrany, R. T.; Gelasco, A.; Christou, G.; Gorun, S. M.; Penner-Hahn, J. E.; et al. Manganese L-Edge X-ray Absorption Spectroscopy of Manganese Catalase from *Lactobacillus plantarum* and Mixed Valence Manganese Complexes. *J. Am. Chem. Soc.* **1996**, *118*, 65–69.

(56) Gilbert, B.; Frazer, B. H.; Belz, A.; Conrad, P. G.; Nealson, K. H.; Haskel, D.; Lang, J. C.; Srager, G.; De Stasio, G. Multiple Scattering Calculations of Bonding and X-ray Absorption Spectroscopy of Manganese Oxides. *J. Phys. Chem. A* **2003**, *107* (16), 2839–2847.

(57) Morales, F.; de Groot, F. M. F.; Glatzel, P.; Kleimenov, E.; Bluhm, H.; Halwecker, M.; Knop-Gericke, A.; Weckhuysen, B. M. In Situ X-ray Absorption of Co/Mn/TiO<sub>2</sub> Catalysts for Fischer-Tropsch Synthesis. *J. Phys. Chem. B* **2004**, *108*, 16201–16207.

(58) de Groot, F. M. F.; Abbate, M.; Elp, J. V.; Sawatzky, G. A.; Ma, Y. J.; Chen, C. T.; Sette, F. Oxygen 1s and Cobalt 2p X-ray Absorption of Cobalt Oxides. *J. Phys.: Condens. Matter* **1993**, *5* (14), 2277–2288.

(59) Nam, K. M.; Shim, J. H.; Han, D.-W.; Kwon, H. S.; Kang, Y. M.; Li, Y.; Song, H.; Seo, W. S.; Park, J. T. Syntheses and Characterization of Wurtzite CoO, Rocksalt CoO, and Spinel Co<sub>3</sub>O<sub>4</sub> Nanocrystals: Their Interconversion and Tuning of Phase and Morphology. *Chem. Mater.* **2010**, *22*, 4446–4454.

(60) Papaefthimiou, V.; Dintzer, T.; Dupuis, V.; Tamion, A.; Tournus, F.; Hillion, A.; Teschner, D.; Havecker, M.; Knop-Gericke, A.; Schlogl, R.; et al. On the Active Surface State of Nickel–Ceria Solid Oxide Fuel Cell Anodes During Methane Electrooxidation. *Adv. Energy Mater.* **2013**, *3*, 762–769.

(61) Wu, Z. S.; Zhou, G.; Yin, L.; Ren, W.; Li, F.; Cheng, H. M. Graphene/Metal Oxide Composite Electrode Materials for Energy Storage. *Nano Energy* **2012**, *1*, 107–131.

(62) Yao, Y.; Xu, C.; Qin, J.; Wei, F.; Rao, M.; Wang, S. Synthesis of Magnetic Cobalt Nanoparticles Anchored on Graphene Nanosheets and Catalytic Decomposition of Orange II. *Ind. Eng. Chem. Res.* **2013**, *52*, 17341–17350.

(63) He, Y.; Chen, W.; Li, X.; Zhang, Z.; Fu, J.; Zhao, C.; Xie, E. Freestanding Three-Dimensional Graphene/MnO<sub>2</sub> Composite Networks as Ultralight and Flexible Supercapacitor Electrodes. *ACS Nano* **2013**, *7* (1), 174–182.